

Mechanistic Understanding and Three-Dimensional Tuning of Fluid Imbibition in Silica-Coated Cotton Linter Paper Sheets

Joanna J. Mikolei, Lukas Neuenfeld, Steffen Paech, Markus Langhans, Markus Biesalski, Tobias Meckel,* and Annette Andrieu-Brunsen*

Paper-based microfluidic devices are used in point of care diagnostic, sensor technology or lab-on-a-chip devices. Although a number of studies has been reported, only relatively few paper-based diagnostic tools are available on the market. A remaining challenge is the mechanistic understanding and precise design of capillary flow in paper. Here, silica coatings are applied to control paper wettability, fiber swelling, and thus fluid transport in all three dimensions of a paper sheet via a simple dip-coating and post-treatment process. By adjusting the three-dimensional silica coating distribution, a three-dimensional asymmetric wettability gradient within the paper sheet is obtained which controls the fluid distribution and imbibition. The correlation between silica coating amount and silica distribution with the resulting fluid behavior is systematically elaborated by analyzing the interaction between fiber and fluid as well as the fiber swelling by applying confocal microscopy. Three different silica-amount dependent fluid distribution states are demonstrated. These new insights into the mechanism of fluid imbibition using simple silica coatings enable the specific design of different imbibition mechanisms and thus the adjustment of the microfluidic properties in paper-based microfluidic devices with control over all three spatial dimensions of a paper sheet in one fabrication step.

(μ PADs). Intensive research has been carried out in point-of-care diagnostics (POC), in particular in the area of lateral flow assays, sensor technology, and lab-on-a-chip implementations. For example, different biomarkers like hormones, DNA, RNA, proteins or different metabolites,^[1] including inflammatory markers such as Interleukin 8,^[2,3] or cancer biomarkers in the context of an early cancer diagnosis,^[4,5] as well as the concentration of glucose in blood, sweat or urine was detected.^[6–13] In addition to medical diagnosis paper-based microfluidic devices are used as sensors for detection of environmental pollution,^[1,14] pesticide detection,^[15] determination of nitrate concentration in water,^[16] or as a sensor to detect heavy metals such as copper, cobalt, nickel, lead or mercury.^[17–25]


Fluid transport control in paper, a key feature for μ PAD design, is to date achieved by either hydrophobic barrier deposition, often using wax or hydrophobic polymer such as polystyrene to adjust the channel width, or secondly by

shaping of the paper fiber itself, and thirdly by adjusting the paper composition.^[1,26–29] To improve fluid mixing, wax pillars printed into the channel have been demonstrated to slow down the fluid flow and to create turbulences whereby a better mixing and distribution is achieved.^[30,31] In a preliminary work of our research group redox gating of fluid imbibition in silica-coated paper sheets has been demonstrated using redox-responsive polymers. These stimuli-responsive polymers allow to switch from fluid exclusion to fluid imbibition.^[32] Further examples demonstrating switching from fluid exclusion to fluid imbibition use PNIPAAm as temperature-responsive coating.^[33,34] These approaches differ in their applicability: Hydrophobizing agents such as wax, polystyrene or PDMS are deposited on the papers using various printing-, stamping, dipping- or spraying processes or even grafting polymerization.^[1,2,5,21,27,35,32,36] Shaping techniques are relatively expensive due to the necessary equipment.^[10,23,35,37–39] Tuning fluid transport through the fiber type, fiber density, or paper grammage bares the advantage of simple integration into existing paper fabrication processes. None of these approaches allows to tune fluid flow in all three dimensions of a paper sheet, although, this would open new possibilities such as sensitivity enhancement and the design of multifunctional microfluidic paper-based devices or asymmetric

1. Introduction

Due to its unique chemical and hierarchically porous structure, fluids can be transported in paper without connecting external pumps. Together with paper originating from renewable resources and being technically produced on a large scale, this results in paper being applied in microfluidic devices

J. J. Mikolei, L. Neuenfeld, S. Paech, M. Langhans, M. Biesalski, T. Meckel, A. Andrieu-Brunsen
Ernst-Berl Institut für Technische und Makromolekulare Chemie
Technische Universität Darmstadt
Alarich-Weiss-Strasse 8, D-64287 Darmstadt, Germany
E-mail: tobias.meckel@tu-darmstadt.de;
annette.andrieu-brunsen@tu-darmstadt.de

 The ORCID identification number(s) for the author(s) of this article can be found under <https://doi.org/10.1002/admi.202200064>.

© 2022 The Authors. Advanced Materials Interfaces published by Wiley-VCH GmbH. This is an open access article under the terms of the Creative Commons Attribution-NonCommercial-NoDerivs License, which permits use and distribution in any medium, provided the original work is properly cited, the use is non-commercial and no modifications or adaptations are made.

DOI: 10.1002/admi.202200064

wettability for paper-based separation and packaging.^[29] More complex sensing concepts are to date realized in so-called Origami and Sudoku paper devices in which the analytes are, e.g., brought into contact with reactants by folding.^[12,15,40–47] This requires a complex arrangement of the individual sensing areas and requires very precise folding to induce contact. Multilayered papers with asymmetric wettability do not need to be folded and asymmetric wettability is to date mainly achieved by one-sided coating, mostly using waxes or polymers, the introduction of nanoparticles, through the design of multilayer systems or by generating nanoscale roughness.^[29,42,44,48–54] In previous studies of our research groups Janus-type paper hybrid materials with an asymmetric wettability along the paper cross-section was achieved using silica coatings and a simple dip coating processes and with a very low amount of silica.^[32,55] How the fluid imbibition speed along such gradients is affected by the gradient design and how three-dimensional gradient formation can be achieved and used for fluid flow design is not yet understood.

Here, we present the design and tuning of a three-dimensional wettability gradient into a cotton linter paper based on tailoring the silica coating distribution along all three spatial dimensions of the paper sheet. Using confocal laser scanning microscopy (CLSM) we observed three states of water distribution inside silica-modified paper sheets depending on the silica amount and distribution. Water can be localized i) at the surface of the fiber, ii) in the fiber lumen, and iii) in the fiber voids. Depending on the localization of the water in the fiber structure, three different imbibition scenarios can be distinguished. Thereby, the silica coating affects the specific surface area as deduced from krypton gassorption measurements. Furthermore, local fluid-imbibition observed with CLSM reveals that the silica coating shields the fibers from the fluid penetration and thus prevents fiber swelling, when reaching a critical silica amount and a specific silica distribution within the paper sheet.

These two parameters, porosity change, and fiber swelling suppression are identified as the main driving forces for wettability and fluid imbibition control using silica functionalization. We additionally demonstrate that the silica gradient direction relative to the fluid imbibition direction can also be used to accelerate or decelerate fluid velocity. By comparing fluid imbibition in un-modified, dense silica-, and mesoporous silica-coated paper sheets, we generate a systematic mechanistic understanding of the fluid flow through silica-coated paper sheets.

2. Results and Discussion

2.1. Analysis of Three-Dimensional Silica Gradient on Cotton Linter Paper

A three-dimensional dense silica gradient is created in a simple dip coating process followed by thermal posttreatment of laboratory-engineered cotton linter paper sheets (**Figure 1**). The silica coating was deposited, by lengthwise dipping of the paper sheets into a sol-gel solution and subsequent withdrawal from that solution by applying a constant withdrawal speed of 2 mm s^{-1} (see the notation of the paper axes and the paper coating process in Figure S1, Supporting Information). The deposited silica amount and the steepness of the silica gradient were adjusted on the one hand by varying the precursor concentration (**Table 1** and **Figure 2**) and on the other hand by the number of repetitions of the dip-coating cycles. After the coating process, the silica-coated paper sheets undergo a temperature treatment. During this curing process, the sheets are aligned horizontally in the oven. This alignment results in a gradient of silica coating distribution along the cross-section of the paper as reported in our previous study.^[55] A gradient along the paper length is additionally introduced through multiple dip-coating cycles. The latter predominantly develops from

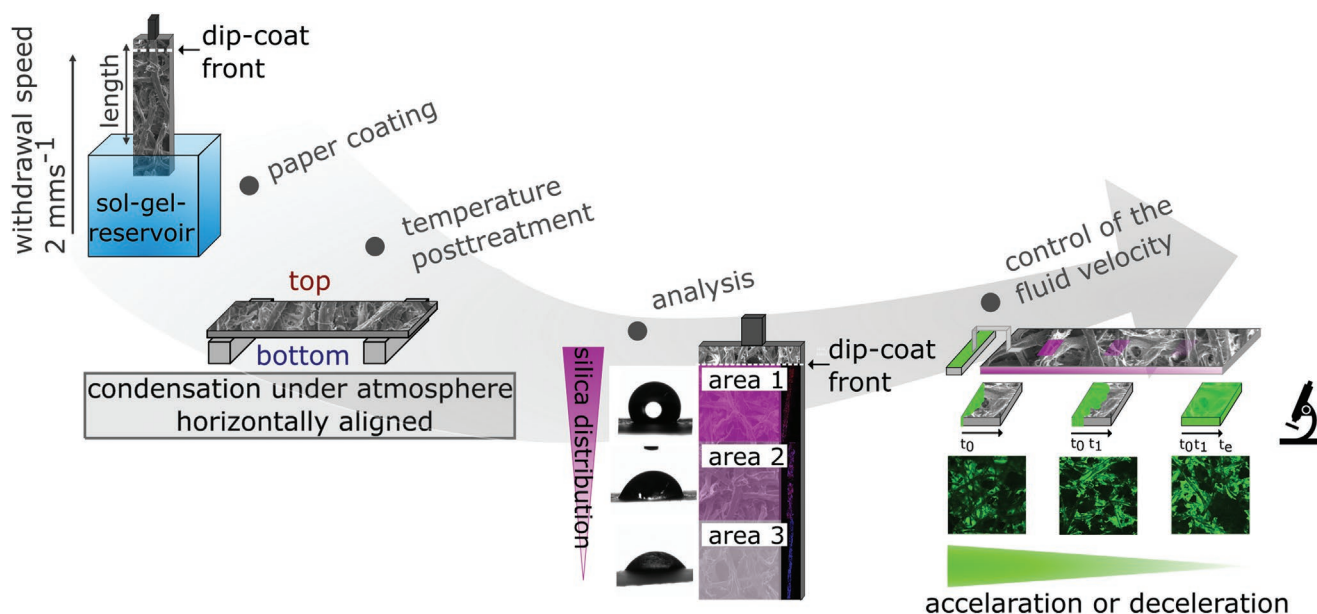


Figure 1. Schematic illustration of the procedure for creating and investigating cotton linter papers with a three-dimensional dense silica gradient coating.

Table 1. Sol-gel solutions for dense and mesoporous silica coating with the following molar ratios according to the published protocols.^[32,55,57]

	TEOS	EtOH	H ₂ O	Conc. HCl	F127
Low concentration	1	80	20	0.04	-
Intermediate concentration	1	40	10	0.02	-
High concentration	1	20	5	0.01	-
Mesoporous sol-gel solution	1	20	5	0.01	0.005

the area close to the dip-coat front (Figure 1) with a high silica amount to the opposite end of the paper sheet with a lower

silica amount. The resulting three-dimensional gradient can be observed independently of the paper grammage and the sol-gel composition (Figure S2 – Figure S9, Supporting Information). This implies, that the formation of the three-dimensional gradient requires a two-step process, namely dip coating and a thermal posttreatment.

To analyze the gradient along the paper length (Figure 1), the paper is divided into three equally sized areas along its length (in the following named: paper areas 1, 2, and 3; Figure S1b, Supporting Information). The silica amount within each area is subsequently determined using thermogravimetric analysis (TGA). With static contact angle measurements (CA) the

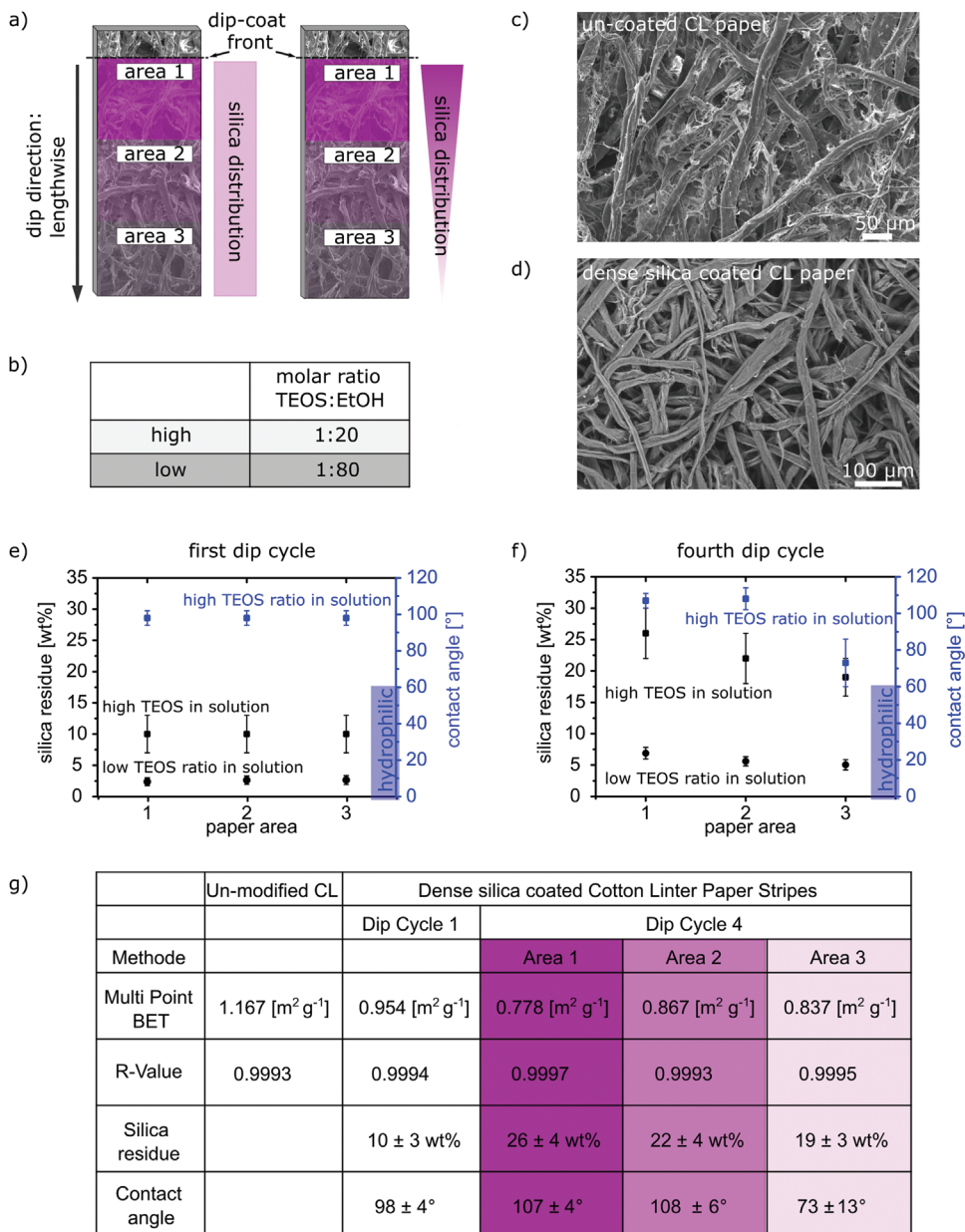


Figure 2. a) Schematic illustration of the paper areas and the dip-coating direction. b) Table with the molar ratios for the high and low concentrated dense silica sol-gel solution; SEM image of an un-coated (c) and silica-coated (d) cotton linter paper sheet. e) and f) Graphical illustration of the influence of the following parameters: number of dip-cycles, TEOS concentration, and paper area on the silica residue and contact angle. g) Summary of silica coating, measured contact angles, and measured specific surface areas with the high concentrated sol-gel solution.

related wettability for each area was analyzed and the changes in the specific surface area due to the coating were determined with krypton gas sorption measurements. CLSM imaging was used to investigate the spatial distribution of the silica coating.

Figure 2e,f,g show the silica amount and the corresponding contact angles after one and four consecutively preformed dip-coating cycles using the high (TEOS ethanol ratio of 1:20) and the low concentrated (TEOS ethanol ratio of 1:80) sol-gel solutions. With increasing the TEOS precursor concentration in the solution, the deposited silica amount increases with each dip-coating cycle (Figure 2e,f,g). A silica amount of 2.5 ± 0.7 wt% is obtained after one dip-coating cycle using the low concentrated sol-gel solution. The high concentrated solution results in a higher silica amount of 10 ± 3 wt%. Both sol-gel solutions showed a uniform dense silica deposition along the paper length after a single dip-coating step (Figure 2e,f). Unlike the single dip-coated samples, a gradient silica distribution along the paper length is obtained when repeating subsequent dip-coating steps. After four dip-coating cycles, a gradual silica distribution along the paper length from area 1 to area 3 with silica amounts of 7 ± 0.9 wt% in paper area 1, 6 ± 0.7 wt% in paper area 2, and 5 ± 0.8 wt% in paper area 3 is obtained in case of the low concentrated sol-gel solution. This is a difference of 2 wt% of deposited silica between paper areas 1 and 3. The silica amount difference can be expressed in a gradient steepness of 0.56 ± 0.44 wt% cm^{-1} (Figure S10, Supporting Information). Applying the highly concentrated sol-gel solution, silica amounts of 26 ± 4 wt% in paper area 1, 22 ± 4 wt% in paper area 2, and 19 ± 3 wt% in paper area 3 are measured after dipping four times. This is a difference of 7 wt% of deposited silica between paper areas 1 and 3. The steepness of the gradient is 1.66 ± 1.32 wt% cm^{-1} which is about the factor of three steeper than the gradient with the low concentrated solution.

Analyzing the resulting wettability reveals, that the paper samples, which were dip-coated one or four times with the low concentrated sol-gel solution, have kept the intrinsic hydrophilic character of cotton linter paper sheets independently of the dense silica gradient. This indicates, that silica of up to 7 wt% is not sufficient to prevent fluid imbibition. The latter changes drastically if silica of more than 10 ± 3 wt% were deposited on the paper fibers. Then water was no longer capable of wicking the pore structure of the paper sheet by capillary action. As a result, a minimum amount of 10 ± 3 wt% deposited silica is required to create a hydrophobic character. This amount of silica coating is not achieved with a one- or four-time dip cycle in a low concentrated sol-gel solution. Contact angles of $98 \pm 3^\circ$ were measured for such papers, rendering the before mentioned silica amount as a critical amount for creating hydrophobic cotton linter paper sheets under the applied conditions. A further change in the measured contact angles is observed along these gradients. Contact angles in the range of $78 \pm 13^\circ$ are obtained on the paper areas with a silica amount of 19 ± 3 wt%. With silica coating of $22 - 26 \pm 4$ wt%, contact angles larger than $108 \pm 6^\circ$ are obtained (Figure 2e,f,g).

With increasing dense silica coating amount, the specific surface area of the paper sheet decreases. Un-modified cotton linter paper sheets with a grammage of 40 g m^{-2} show a specific surface area of $1.167 \text{ m}^2 \text{ g}^{-1}$ (Figure 2g) as determined by Krypton adsorption and BET model. A coating with 10 wt%

reduces the specific surface area to $0.954 \text{ m}^2 \text{ g}^{-1}$ (Figure 2g). The gradual silica distribution after four dip-coating cycles with the high concentrated sol-gel solution is also reflected in a further gradual specific surface area reduction. Specific surface areas of $0.778 \text{ m}^2 \text{ g}^{-1}$ in paper area 1 (26 ± 4 wt% dense silica), $0.867 \text{ m}^2 \text{ g}^{-1}$ in paper area 2 (22 ± 4 wt% dense silica), and $0.837 \text{ m}^2 \text{ g}^{-1}$ (19 ± 3 wt% dense silica) in paper area 3 are detected (Figure 2g). This further specific surface area reduction is less pronounced between uncoated and once dip-coated paper sheets. It has to be noted, that the decrease of specific surface area is most significant after the first dip-coating step. SEM images give insight into the reason for the pronounced or less pronounced reduction of the surface area with an increasing amount of the silica coating. The surface of un-coated cotton linter fibers is rough and the voids are filled with fibrils which are detached from the fiber bundle (Figure 2c). The fiber surface of silica-coated fibers appears very smooth and no fibrils are sticking out (Figure 2d). As a result, the voids between the fibers are larger and more open for coated papers and fibril swelling is probably not contributing anymore to fluid imbibition. This reduction of fibrils results in the lower specific surface area of these papers as compared to uncoated papers.

To understand and rationalize the role of dense silica coating distribution in cotton linter paper CLSM fluorescence microscopy was used. In order to visualize the coating distribution by fluorescence, rhodamine B was added to the silica forming sol-gel solutions. The cotton linter fibers were stained with calcofluor white (CFW) prior to the silica coating. Paper sheets were visualized in the xy -plane as well as along their z -plane recording z -stacks (Figure S13, Supporting Information). It must be noted that a z -stack recording through the entire cross-section of the paper sheet would come with image quality losses mainly due to light scattering and signal attenuation. Thus, information on the silica distribution along the paper cross-section has been obtained by embedding the sample in a resin mixture and cutting cross-sections using a microtome. Subsequently, the intensity values of the pixels recorded via CLSM were analyzed for the rhodamine B dye. A high intensity indicates a high amount of silica coating.

A homogenous silica distribution along the paper length is investigated at the paper sheet top surface after one single dip coating step (Figure 3g–i). This is expected from the TGA results (Figure 2g). Surprisingly, a constant distribution is observed for the top surface of the paper sheets after four dip-coating steps (Figure 3j–l), too. This seems to contradict the TGA results, which indicate a silica gradient along the paper length with increasing silica amount from area 3 to area 1. These results indicate that the coating on the top surface of the paper sheet is homogeneous, whereas the silica gradient distribution occurs along the paper cross-section (TGA results Figure 2f,g). The CLSM cross-section analysis of paper sheets coated with a single dip-coating step clearly confirms a uniform silica distribution as expected (Figure 3m,o). Whereas, the CLSM images of the paper cross-sections after four dip-coating cycles confirm the gradient silica distribution (Figure 3n,p). Consequently, after four dip-coating steps a three-dimensional gradient along the paper cross-section is obtained, which in addition varies regarding silica amount along the length of the paper sheet.

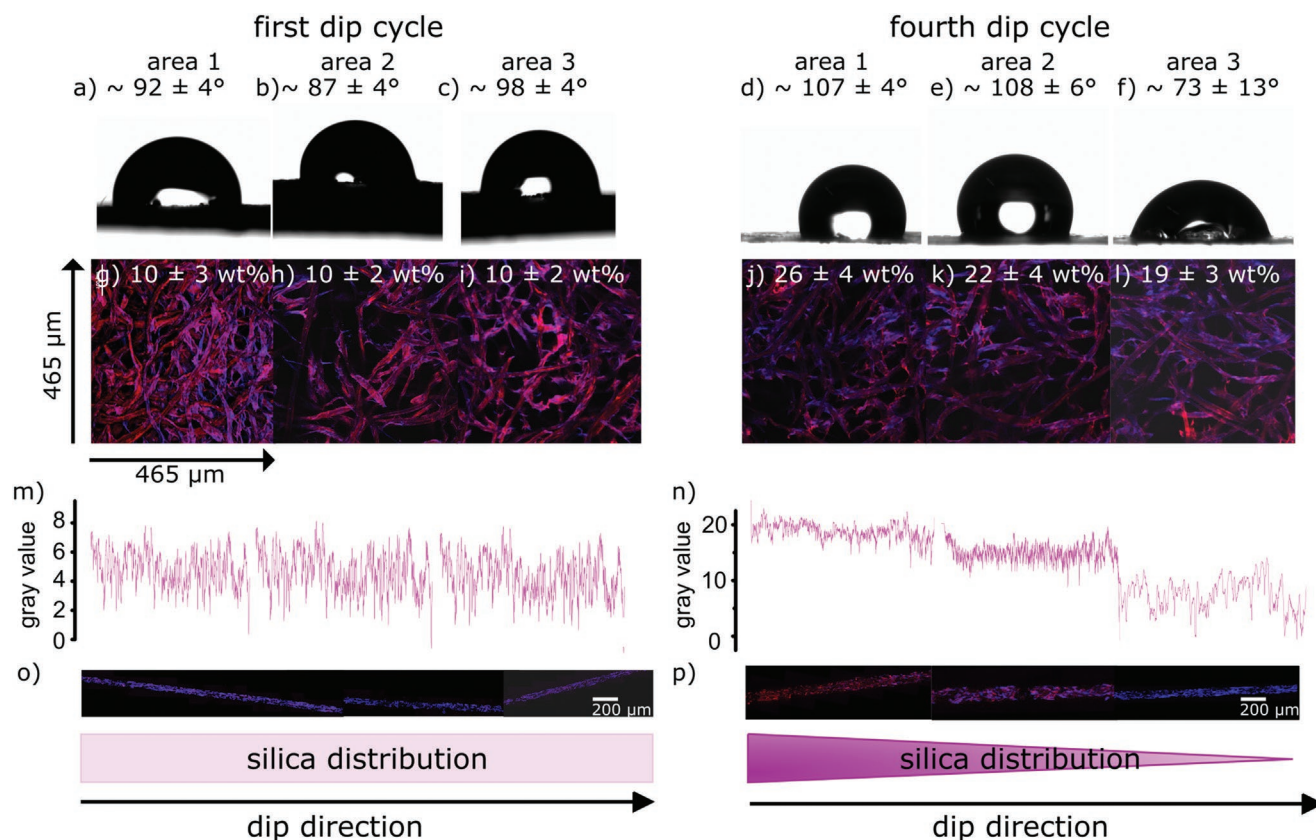


Figure 3. The static contact angles of 2 μL water droplet at the three paper areas of one-time a–c) and four-time d–f) dip-coated samples using the high concentrated sol-gel solution; CLSM images of the top side from the one-time g–i) and four-time j–l) dip-coated sample; Plot of the mean gray values along the paper length (from left to right) of the cross-section from the one-time (m) and four-time (n) dip-coated samples; CLSM images of the cross-section from the one-time (o) and four-time (p) dip-coated paper samples.

From the obtained data it can be concluded, that the distribution of the silica coating depends on an interplay between capillary transport and the evaporation process and that this gradient distribution can be adjusted based on the initial TEOS precursor concentration and the number of performed coating steps. Transport of sol-gel solution due to evaporation seems to overlay with transport of sol-gel solution via capillary forces during the evaporation process. As a result, more silica accumulates in areas 1 and 2 of the paper samples during the dip-coating process. The gradient along the cross-section of the paper sheet is probably caused by different evaporation rates at the bottom and the top of the paper sheet during the curing process, as demonstrated in our previous study comparing curing at different pressures.^[55]

2.2. Tuning the Fluid Imbibition by Influencing the Interaction Between Fluid and Fiber Due to Different Silica Coatings

Fluid imbibition in paper is influenced by different parameters, such as pore structure, surface energy, or viscosity of the fluid. An essential parameter that is often neglected when probing fluid imbibition with paper sheets is the fiber swelling. The degree of fiber swelling depends therefore not only on the fiber type, but also on the accessibility of the fiber for the fluid.

In order to understand the influence of the dense or mesoporous silica coating on the wettability, fluid imbibition, and fluid distribution in paper, the fluid imbibition into different silica-coated cotton linter paper sheets was analyzed using CLSM. Therefore, the samples were horizontally aligned and a defined volume of 30 μL aqueous FITC-Dextran 70 solution was applied at one end of the paper sheet (Figure S14, Supporting Information). CLSM images were recorded from the bottom side of the paper sheet. The fluid imbibition along the paper length was visualized in the xy -plane of a single image section depending on the time (Figure S14, Supporting Information). This setup allows to investigate the distribution and localization of the fluid in the paper next to the imbibition velocity and the maximum imbibition distance for a fluid volume of 30 μL .

Next to paper samples with different amounts of dense silica coatings, cotton linter papers with a mesoporous silica coating were investigated. The difference between both coatings is the presence of nanoscale pores in the mesoporous silica coating (see the experimental section for fabrication details).

When investigating the imbibition mechanism, the following three scenarios were distinguished: In the first scenario without or with very low silica amount, the fluid flows along the fiber wall and inside the fiber lumen (Figure 4a). This first scenario (I) is accompanied by fiber swelling due to liquid

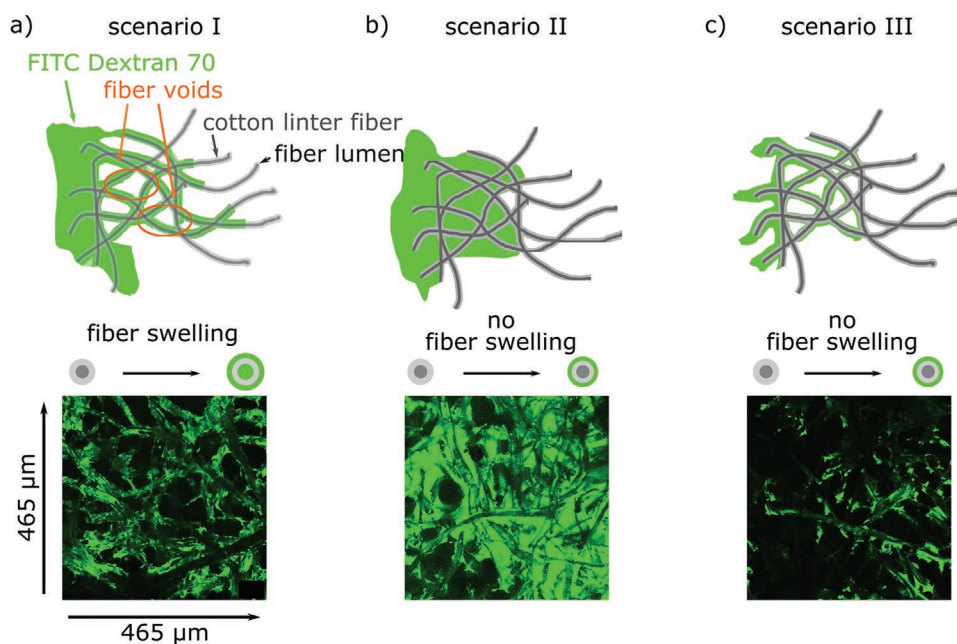


Figure 4. a) Illustrates the imbibition scenario I in which the fluid is localized on and in the fiber. b) Illustrates the imbibition scenario II in which the fluid fills the voids between the fibers without penetrating the inner part of the fiber. c) Illustrates the imbibition scenario III in which the fluid is located at the outer surface of the fiber and no fiber swelling occurs.

fiber penetration. In the second scenario (II), the fluid fills the voids between the fibers before the fluid front continues and no fiber swelling seems to occur (Figure 4b). In the third scenario (III), the fluid flows along the fiber outer surface without fiber swelling or filling the fiber lumen and without filling the fiber voids in between the fibers (Figure 4c). Even higher silica amount results in water exclusion and hydrophobic paper sheets (Figure 2e,f). Through the targeted use of silica coatings (silica amount, homogenous, gradual or mesoporous silica coatings), the three different scenarios can be generated. This also allows to adjust the fluid imbibition velocity. This is caused by the effects of different silica coatings on the specific surface area of the paper, on the structure of the fiber surface, as well as the control of the fluid accessibility to the fiber. In general, a lower and smoother surface (scenario II and III compared to scenario I) leads to a deceleration of the fluid velocity. A high dense silica coating amount prevents fiber swelling (scenario II and III). This leads to an acceleration of the flow compared to scenario II, although the specific surface area is smaller and smoother. By selectively adjusting fluid imbibition mechanisms via the corresponding coating amount and silica coating distribution, the imbibition in paper can be controlled.

More specifically, un-modified cotton linter paper sheets with a grammage of 40 g m^{-2} show an imbibition mechanism of scenario I (Figure 4a). The imbibition along the fluid front is characterized by a fast and uniform fluid flow. The fluid is mainly localized on the inner and outer fiber surface. At the fluid front no fluid is located in the voids between the fibers. Due to the interaction between the liquid with the fiber and the resulting fiber swelling, the fluid rapidly flows along the fiber network, whereby not all fibers and fibrils are used (Figure 4a and Figure 5a). With increasing distance from the fluid contact zone (Figure S14, Supporting Information), the imbibition

velocity decreases, and the fluid becomes mostly located at the outer surface of the fibers (Figure 4c and Figure 5b,c). The lumen of the fiber is no longer used for the fluid transport (Figure 5c paper area 3). This predominant presence of water in the fiber wall indicates, that the driving force for fluid imbibition under these conditions are provided by fiber swelling.

Using mesoporous silica in the coating process, in contrast to dense silica as discussed above, the fluid distribution corresponds to scenario I and thus resembles the fluid distribution of un-coated cotton linter paper sheets. In mesoporous silica-coated papers, the fluid is located at the inner and outer surface of the fiber, as well as in the fiber lumen and fiber swelling occurs (Figure 5e). Interestingly, the imbibition velocity is faster for mesoporous coated samples as compared to un-modified paper even though the CLSM images show the same fluid distribution (Figure 5a,e). This faster imbibition might be caused by an additional fluid transport in the mesopores of the silica coating (Figure 5j).

Scenario II was realized with homogeneously dense silica-coated paper sheets with a coating amount of $10 \pm 3 \text{ wt}\%$. These paper sheets show an interconnected fiber network with smooth fiber surfaces, no detached fibrils, and fibril-free voids between the fibers (Figure 5b,g). Compared to the un-modified paper, the fluid is mainly located in the voids between the fibers and less in the fiber itself. A fluid penetration into the fiber inner surface and thus a fiber swelling is not observed. The fluid transport is characterized by a step-wise fluid front propagation. This indicates a different imbibition mechanism as compared to scenario I. The fluid front advances a certain distance along the fiber outer surface followed by filling of the voids between the fibers. Only after void filling, the fluid front further advances a certain distance along the fiber surface.

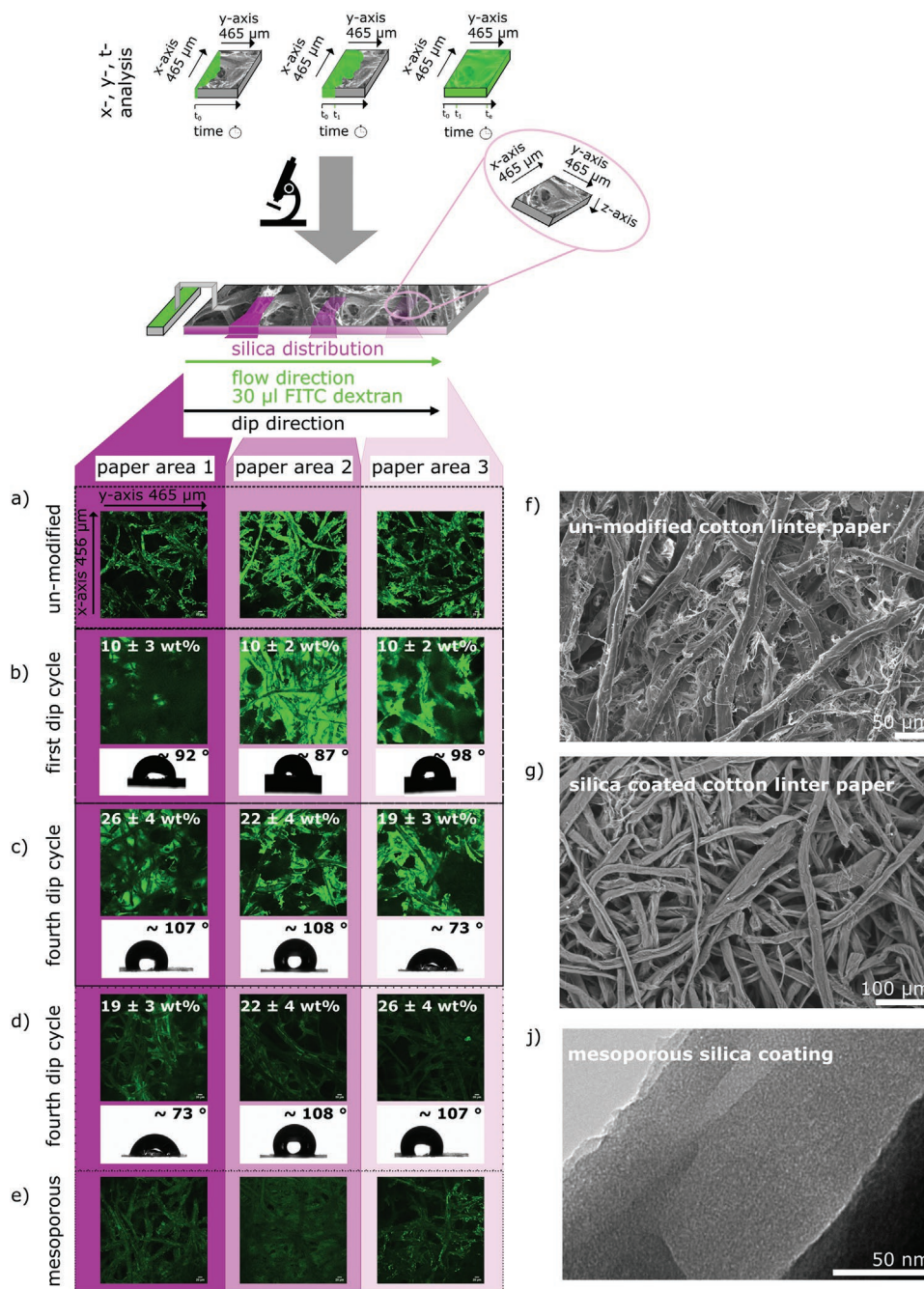


Figure 5. The fluid distribution in the three different paper parts of: a) un-modified samples with a specific surface area of $1.167 \text{ m}^2 \text{ g}^{-1}$; b) one-time dip-coated samples with a silica content of 10 wt% and a surface area of $0.954 \text{ m}^2 \text{ g}^{-1}$; c) four-time dip coated cotton linter papers with a silica gradient along the paper length from high to low silica; d) same as c with inverse flow direction; e) mesoporous silica-coated cotton linter paper. f) SEM image of an uncoated paper. g) SEM image of silica-coated paper. j) TEM image revealing the mesoporous nature of the silica coating on top of the cotton linter fibers upon heat treatment at $500 \text{ }^\circ\text{C}$.

This imbibition is significantly slower than the fluid transport along the inner and outer fiber surfaces. The reduced imbibition speed is probably caused by fiber swelling and the complete filling of the voids between the fibers before further propagation. Due to these two mechanistic phenomena, a relatively large volume of liquid is taken up by the paper sheet which slows down the flow velocity. With increasing distance between fluid front and fluid reservoir, the flow velocity slows

down more and more. Because of the liquid is no longer filling the voids completely, the fluid front continues along the fiber surface until the flow stops which resembles a transition to scenario III. At this point, the capillary forces originating from the inter-fiber porosity are no longer sufficient to cause further fluid flow of the limited fluid volume. These observations are in agreement with a study of Bump et al. describing the fluid flow in P(MMA-co-MABP-co-RhBMA) coated cotton linter paper.^[56]

This study already indicated that the wetting front under the reported conditions is mainly localized at the fiber surface and is followed by the remaining imbibition. The localization of the wetting front complies with the scenario II in our results (Figure 4c).

Paper with a three-dimensional silica gradient along its length and cross-section (from 26 ± 4 wt% to 19 ± 3 wt%) combines imbibition scenario III and I. In the paper area with high silica content, paper scenario III can be observed. In contrast, scenario I is observed in the paper areas with a lower silica amount (paper areas 2 and 3).

Please note that the fluid contact is established via a paper bridge between the $30 \mu\text{L}$ fluid reservoir and the top surface of the paper sheet in paper area 1. The top surface of the paper sheet shows an identical silica content along the paper area 1 to paper area 3 along the paper length (Figure 3g–i, j–l). The CLSM images are recorded from the bottom side, which is expected to show different silica content in area 1 to area 3 compared to the top side as the gradient occurs along its cross-section. Consequently, the steepness of the cross-section gradient decreases from paper area 1 to paper area 3. The liquid distribution and imbibition in paper area 1 correspond to scenario III. When the liquid flow continues in the paper areas 2 and 3 with less silica coating as compared to paper area 1, the fluid is mainly located at the inner and at the outer fiber surface which corresponds to scenario I.

Depending on the fluid flow direction, from the paper area with high silica coating amount (paper area 3) to the paper area with low silica amount (paper area 1) or vice versa, the imbibition velocity but not the water distribution is affected. A faster flow is obtained when the fluid contact is located at the top side of paper area 1 containing a lower silica amount. Realizing fluid flow towards the high coated paper area 3 is faster in comparison to the reverse imbibition direction.

For comparison of the imbibition velocity and total imbibition distance of the differently coated samples, absolute timepoints of fluid appearance at a specific travel distance (Figure 6) were extracted from metadata of the confocal recordings (Figure S14,

Supporting Information). The obtained curves underline the influence of coatings on the imbibition mechanisms. Fast imbibition velocities are obtained for silica-coated paper sheets in which water distribution according to scenario I and III of Figure 4 is observed. The fluid flow at the inner and outer fiber surface as well as fiber swelling are the strongest driving forces for fluid imbibition resulting in the fastest fluid transport.

This is the case for un-modified cotton-linter papers (Figure 6 dark orange curve), cotton linter papers with a three-dimensional silica coating (Figure 6 ranging from nearly uncoated to highly coated paper areas at the bottom side, dark and light blue curve), and mesoporous silica coating (Figure 6 violet curve). In contrast, the imbibition scenario II which occurs in homogeneously coated samples (Figure 6 gray curve) leads to a slower imbibition velocity and shorter averaged imbibition distance. Interestingly, these different imbibition scenarios are only observed in the horizontally preformed imbibition experiments with a water delivery via a paper bridge (Figure S14, Supporting Information). If the hydrophobic paper samples (CA between 73° and 108°) are vertically placed in a water reservoir, no imbibition was observed (Figure S15, Supporting Information). Clearly, compared to the horizontally performed imbibition experiments, the imbibition has to overcome the gravitational force in the vertically performed experiments. On one hand, this may imply that the capillary force is lower than the gravitational force. On the other hand, the delivery via a paper bridge may feed the water differently into the complex capillary system of these papers, thereby promoting the transport of water. Furthermore, an acceleration of the imbibition compared to unmodified cotton linter samples can be achieved by introducing mesopores into the silica coating (Figure 6 violet curve). This coating does not prevent fiber swelling. In addition to the fluid transport in and on the fiber, a fluid transport very probably takes place in the mesopores which provide a significant capillary force and specific surface area. Scenarios I and III do not only result in a fast imbibition velocity. They also ensure a longer averaged imbibition distance for the $30 \mu\text{L}$ fluid volume with 25 mm for mesoporous silica-coated paper.

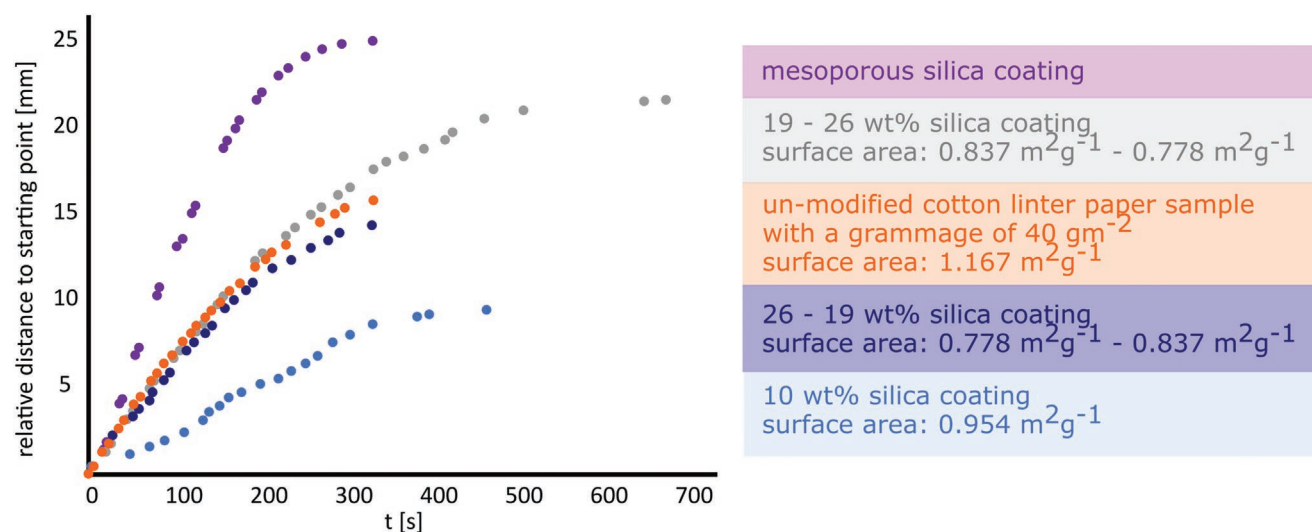


Figure 6. The imbibition velocity along the paper length of paper samples which are un-modified or which are modified with different silica coating amounts.

For un-modified paper sheets, an average imbibition distance of 16 mm for a fluid volume of 30 μL is observed. With mesoporous silica coating, the averaged imbibition distance is nearly doubled compared to the un-modified papers. Paper samples with a silica gradient also show an accelerated imbibition compared to un-modified samples in case the flow is directed from the area with lower silica coating amount (area 1) to the maximum silica amount (area 3).

By combining imbibition mechanism I and III, the second fastest imbibition speed is achieved and an averaged imbibition distance of 22 mm is obtained. When flowing through these samples in a reverse manner (from high silica content to a low amount) a slower imbibition velocity and a shorter averaged imbibition distance with 14 mm is obtained (Figure 6 dark blue curve). This implies that fiber swelling accelerates imbibition and preventing fiber swelling slows down imbibition. Homogeneously coated paper sheets (scenario I) show a decrease in fluid imbibition speed and distance compared to un-modified papers. This indicates a reduction in the driving force of fluid imbibition resulting from the interfiber voids.

These findings show, that the use of the Lucas Washburn equation is often not sufficient to describe imbibition process in paper devices. Since the mean pore radius in this equation is usually related to the inter-fiber voids and, as shown by our data, fluid imbibition is not necessarily and not exclusively determined by the filling of the interfiber space. Fiber and fibril porosity as well as fiber swelling have to be considered by a rational fluid imbibition design.

3. Conclusion

In summary, we presented a fabrication strategy to realize three-dimensional silica gradients into cotton linter paper sheets by using consecutive dip-coating and curing. Varying the dip-coating solution composition and performing consecutive dip-coating steps, the amount of silica and the steepness of the silica gradient along the paper length was tuned between 2.5 ± 0.7 wt% and 26 ± 4 wt%. CLSM images of the gradual three-dimensional silica distribution show a homogeneous silica distribution on the paper top side during curing but a gradually varying silica distribution along the paper length (paper area 1 to 3) and cross-section. This silica coating gradient resulted in gradual tuning of wettability. The change between hydrophilic and hydrophobic is depending on a critical amount of silica. A hydrophobic character is obtained for a silica of at least 10 ± 3 wt%. With higher coating amounts, the hydrophobic character increases, and contact angles up to 108° are achieved. In accordance with the wettability, the fluid imbibition velocity can be decelerated or accelerated compared to un-coated cotton linter papers. Depending on the silica coating amount three different water imbibition scenarios have been observed: Water can be localized i) at the surface of the fiber, ii) in the fiber lumen and iii) in the fiber voids. Depending on the localization of the water in the fiber structure, three different imbibition scenarios have been distinguished directly affecting the imbibition speed. Mechanistically a deceleration of water imbibition as compared to un-modified cotton linter paper sheets is observed for scenario II and can be explained

by a smaller surface area and absence of fiber swelling. In addition, the water distribution is preferably located on the fiber surface and not in the voids between the fibers. An acceleration of the fluid can be achieved by inserting a mesoporous silica layer with a simple dip coating process. With a mesoporous coating, fiber swelling occurs and in addition, the fluid flow is channeled in a certain direction. These precise adjustments of the flow make gradual silica-coated papers interesting for lateral flow assays or lab-on-a-chip applications.

4. Experimental Section

Reagents: All chemicals and solvents were purchased from Merck, Sigma-Aldrich, or Alfa Aesar and used as received unless otherwise stated.

Paper Fabrication: For the preparation of lab-engineered paper substrates, cotton linter fibers (curl: 18.7 %, fibrillation degree: 1.6 %, fines content: 37.1 %) were used which were provided by the Eifeltor Mühle factory. The cotton linter pulp was refined in a Voith LR 40 laboratory refiner with an effective specific energy of 200 kWh t^{-1} . From these pulp lab-engineered paper sheets with a grammage of $40 - 43 \text{ g m}^{-2}$ were fabricated using a conventional Rapid-Koethen hand sheet maker according to DIN 54358 and ISO 5269/2 in absence of additives and fillers.

Dense and Mesoporous Silica Coating: Dense and mesoporous silica coatings were synthesized via sol-gel chemistry based on the precursor tetraethoxysilane (TEOS) in analogy to our previous studies.^[55,32] In addition to the precursor TEOS, the template Pluronic F127 was added for the fabrication of mesoporous silica coatings. The preparation of the coating solution was carried out with the respective ratios and were stirred at room temperature for 24 h.

Cotton linter paper stripes with a dimension of $1 \times 5 \text{ cm}$ were dip-coated with the different sol-gel solutions in a climate chamber (Binder APT.line TM KBF E5.2) adjusted to a relative humidity of 50 ± 5 % and a temperature of $25 \pm 1^\circ\text{C}$. For the dip-coating procedure, a withdrawal speed of 2 mm s^{-1} was used and the dip-coating procedures were performed either once as well as in several consecutive cycles for each individual paper stripe. For multiple consecutively performed coating cycles paper stripes were dip-coated several times without a temperature program between the different dip-coating cycles. After the dip coating process with dense silica (no addition of Pluronic F127), the paper sheets were placed into an oven (Carbolite) being horizontally aligned. Freshly deposited mesoporous films were stored in the climate chamber under normal conditions for one hour before being transferred into an oven. Subsequently, a thermal treatment was carried out starting with a temperature increase from 25 to 60°C in 10 min. The temperature of 60°C was kept for 1 h, followed by a second temperature increase from 60 to 130°C in 10 min. The final temperature of 130°C was kept for 2 h before cooling down to ambient temperature by waiting. After the thermal treatment, the template in mesoporous silica-coated cotton linter paper samples was chemically extracted by placing the samples into an acidic ethanol bath (0.01 M HCl) for three days. During all process steps the top of the horizontally aligned samples in the oven were marked and can be identified after the silica-paper hybrid material fabrication.

No silica nanoparticles are formed in the sol-gel solution which were made under the described procedure.

Thermogravimetric Analysis (TGA): TGA analysis was performed on a TGA 1 instrument from Mettler Toledo and the evaluation of the obtained curves was performed with the corresponding program Star1. The paper samples were divided lengthwise into three equally sized parts (Figure S16, Supporting Information). The samples of each paper area were separately analyzed by placing them in $100 \mu\text{L Al}$ crucibles. After placing the samples in the crucible, the samples were heated from 25 to 600°C at a rate of $10^\circ\text{C min}^{-1}$ under constant airflow of 30 mL min^{-1} . The maximum temperature of 600°C was maintained for 10 min.

Contact Angle Measurement (CA): The contact angle measurement was carried out using a Model TBU90E from DataPhysics Instruments GmbH with the corresponding software. For the macroscopic static contact angle measurements, a water droplet with a volume of 2 μL with a dosing rate of 1 $\mu\text{L s}^{-1}$ was applied to the sample surface. The contact angle is measured at three different positions at each individual sample (Figure S17, Supporting Information) generating a mean value and its error.

Scanning Electron Microscopy (SEM): SEM images were obtained by using a Zeiss ECO 10 scanning microscope operating at an acceleration voltage of 20 kV or 10 kV in a high vacuum or in an extended pressure mode. Depending on the selected mode, the samples were analyzed with or without a 10 nm thick platinum(80)/palladium(20) (from ESG Edelmetall-Service Rheinstetten; charge number IN0145660) layer which was applied with a sputter coater (Cressington 208HR).

Confocal Laser Scanning Microscopy Analysis of Silica Distribution: To analyze the silica distribution along cellulose fibers in paper cross-section the samples (cellulose fibers) were first stained with calcofluor white (CFW). The fluorescence labeling of the fibers with CFW was achieved by dipping the untreated papers in an ethanolic (abs.) solution of 10 \times 10 μm CFW. The staining process took place at a relative humidity of 50 \pm 5 % and a temperature of 25 \pm 1 $^{\circ}\text{C}$. A withdrawal speed of 2 mm s^{-1} was used for the staining. After drying at 40 $^{\circ}\text{C}$ in a vacuum oven (Binder) for 1 h, the CFW-stained paper samples were subsequently coated with dense silica (ethanol TEOS ratio 1:20) as described above. Thereby, 1 μm rhodamine B was added to the respective dip coating solution, allowing visualization of the silica coating by fluorescence in CLSM. One single dip coating cycle and four consecutive dip-coating cycles were performed. The dense silica coating is stabilized using the temperature treatment described above.

Before preparing the cross-sectional cuts using a microtome (minot-microtome typ 1212 from E. Leitz) the dense silica-coated paper stripes were divided in three equal-sized pieces (Figure S1b, Supporting Information) and the three paper parts were embedded in a commercial polyurethane resin containing 49.875 wt% Desmodure 3200, 49.9875 wt% Albodure 956 VP and 0.025 wt% TIB-KAT 318. For curing, the embedded samples are stored for 24 h at room temperature. The semiflexible sample was cut into 30 μm thick sections using a microtome. During all these steps, the identity of the sample "top" side und upper part was tracked.

The silica distribution of the paper cross-section along the paper sheet length (for the paper axis notation see Figure S1a, Supporting Information) was analyzed via CLSM imaging. The 30 μm thick paper slices were placed between two microscope cover glasses with a thickness of No. 1.5 (VWR Borosilicate cover glass) together with immersions oil (Typ F Leica) for optical matching. The cover glasses with the sample were placed in a sample holder and the imaging was performed using 20x water and 63x water objectives (Leica) the Leica TCS SP8. Because of the sample size, several images were recorded and combined together to obtain complete information along the paper length. For each image, stacks with a defined step size were recorded. The CLSM images which were recorded in the described manner were processed in the software Fiji.^[58] The CLSM image stacks were summed up to condense the information about the material distribution and a grey value analysis was performed. The gray value of all pixels in the defined area were determined whereby the silica distribution could be analyzed (Figure S13, Supporting Information).

Fluid Flow Analysis with Confocal Laser Scanning Microscopy Imaging: The fluid flow in un-modified as well as in mesoporous and dense silica-coated cotton linter papers were investigated by xyt-imaging using a Leica TCS SP8 microscope with the 8000 Hz resonant scanner. The paper samples for fluid flow analysis were prepared as described before. In order to be able to apply and evaluate a method of analysis, a defined fluid channel with a width of 2 mm was created via wax printing (ColorQubeTM8570, XEROX) on the paper sample. After wax printing paper stripes were heated up on a heating plate (95 $^{\circ}\text{C}$) for a few seconds so that the wax could imbibe into the papers. The printed paper stripes were clamped in a measuring chamber and a paper bridge

was stretched from the fluid reservoir onto the sample (Figure S14, Supporting Information). As fluid, a 30 μL FITC-Dextran 70 solution with a concentration of 0.1 mm was used. FITC was excited with a wavelength of 488 nm and the detection of the emission was carried out at a wavelength of 505 – 525 nm. For detection of rhodamine B and FITC photomultiplier and hybrid detectors were used respectively. To analyze the dynamics of fluid imbibition, the fluid flow was recorded with 14.75 fps in an image section of 465 μm \times 465 μm (512 \times 512 pixels) which are located in the middle of the paper sample. The first measuring point was located 2 mm after the paper bridge. After the fluid has passed the image size, the recording was stopped and the subsequent image section on the paper strip was investigated in the same way. In this way, videos were taken along the entire paper strip until the fluid flow is stopped. In the following evaluation and plotting, the total flow distance is made up of the individual recorded image sections and the empty fields (Figure S14, Supporting Information). The captured flow videos were analyzed using ImageJ.

Krypton Adsorption: Surface area determination was performed using krypton gas sorption at 77 K in a relative pressure range of 0.05 to 0.3 using an Autosorb iQ of Quantachrome. Before measuring, the samples were degassed at 80 $^{\circ}\text{C}$ for 12 h at a high vacuum. The measured adsorption isotherms were evaluated based on the Brunauer-Emmet-Teller (BET) model using the program ASiQwinTM.

Data Reproduction: The obtained analytical data for example the TGA and contact angle measurements were directly used for the evaluation without any further data manipulation. From this original data analysis as described in the corresponding characterization experimental section, each mean value and error bar given in the manuscript is based on five to ten reproduction experiments in material fabrication and subsequent characterization. A krypton gas sorption measurements are based on at least four to five reproduced material fabrication paper sheet sections due to the required material amount. CLSM REM and TEM images have been performed on selected samples.

In all the figures and tables, the main value and the standard deviation is indicated which were calculated using the following formula using excel or origin as software.

mean value:

$$\bar{x} = \frac{1}{n} \sum_{i=1}^n x_i \quad (1)$$

x is the experimental data and n is the number of experiments which were performed with the same parameters

standard deviation:

$$\sigma(x) = \sqrt{\sum_{i=1}^n (x_i - \bar{x})^2} \quad (2)$$

σ is the standard deviation

x is the experimental data

n is the number of experiments which were performed with the same parameters

Supporting Information

Supporting Information is available from the Wiley Online Library or from the author.

Acknowledgements

The authors kindly acknowledge the financial support by the German Research Foundation (DFG) in the project AN1301/8 and acknowledge the DFG PAK-962. In addition, the authors thank Ulrike Kunz for TEM measurements, Mark Höfler and Dr. T. Gutmann for the solid-state NMR measurements, Alexander Ritter von Stockert for providing the

cotton linter pulp material, Prof. S. Schabel and Christiane Helbrecht for supporting with the cotton linter fibers treatment and refining, the Merck Lab for access to SEM.

Open access funding enabled and organized by Projekt DEAL.

Conflict of Interest

The authors declare no conflict of interest.

Data Availability Statement

The data that support the findings of this study are available from the corresponding author upon reasonable request.

Keywords

imbibition control, paper-based hybrid materials, paper-based microfluidic devices

Received: January 11, 2022

Revised: March 2, 2022

Published online: June 1, 2022

- [1] E. Noviana, T. Ozer, C. S. Carrell, J. S. Link, C. McMahon, I. Jang, C. S. Henry, *Chem. Rev.* **2021**, *121*, 11835.
- [2] M. Gutiérrez-Capitán, A. Baldi, C. Fernández-Sánchez, *Sensors (Basel)* **2020**, *20*, 967.
- [3] M. Jauset-Rubio, M. Svobodová, T. Mairal, C. McNeil, N. Keegan, A. Saeed, M. N. Abbas, M. S. El-Shahawi, A. S. Bashammakh, A. O. Alyoubi, C. K. O Sullivan, *Sci. Rep.* **2016**, *6*, 37732.
- [4] N. Fakhri, S. Abarghoei, M. Dadmehr, M. Hosseini, H. Sabahi, M. R. Ganjali, *Spectrochim. Acta, Part A* **2020**, *227*, 117529.
- [5] J.-Y. Huang, H.-T. Lin, T.-H. Chen, C.-A. Chen, H.-T. Chang, C.-F. Chen, *ACS Sens.* **2018**, *1*, 174.
- [6] W. Dungchai, O. Chailapakul, C. S. Henry, *Anal. Chem.* **2009**, *14*, 5821.
- [7] C. Zhao, M. M. Thuo, X. Liu, *Sci. Technol. Adv. Mater.* **2015**, *4*, 49501.
- [8] H. Zhang, E. Smith, W. Zhang, A. Zhou, *Biomed. Microdevices* **2019**, *3*, 48.
- [9] G. Xiao, J. He, X. Chen, Y. Qiao, F. Wang, Q. Xia, L. Yu, Z. Lu, *Celulose* **2019**, *7*, 4553.
- [10] E. L. Fava, T. Martimiano do Prado, T. Almeida Silva, F. Cruz de Moraes, R. Censi Faria, O. Fatibello-Filho, *Electroanalysis* **2020**, *5*, 1075.
- [11] A. Gonzalez, L. Estala, M. Gaines, F. A. Gomez, *Electrophoresis* **2016**, *12*, 1685.
- [12] D. Sechi, B. Greer, J. Johnson, N. Hashemi, *Anal. Chem.* **2013**, *22*, 10733.
- [13] A. Böhm, S. Trosien, O. Avrutina, H. Kolmar, M. Biesalski, *Front. Chem.* **2018**, *6*, 214.
- [14] J. Qi, B. Li, X. Wang, L. Fu, L. Luo, L. Chen, *Anal. Chem.* **2018**, *20*, 11827.
- [15] F. Arduini, S. Cinti, V. Caratelli, L. Amendola, G. Palleschi, D. Moscone, *Biosens. Bioelectron.* **2019**, *126*, 346.
- [16] A. Charbaji, H. Heidari-Bafroui, C. Anagnostopoulos, M. Faghri, *Sensors (Basel)* **2020**, *21*, 102.
- [17] R. Ding, Y. H. Cheong, A. Ahamed, G. Lisak, *Anal. Chem.* **2021**, *4*, 1880.
- [18] X. Weng, S. Neethirajan, *Microchim. Acta* **2017**, *11*, 4545.
- [19] J. Zhou, B. Li, A. Qi, Y. Shi, J. Qi, H. Xu, L. Chen, *Sens. Actuators, B* **2020**, *305*, 127462.
- [20] R. Ding, V. Krikstolaityte, G. Lisak, *Sens. Actuators, B* **2019**, *290*, 347.
- [21] P. Kamnoet, W. Aeungmaitrepirom, R. F. Menger, C. S. Henry, *Analyt.* **2021**, *7*, 2229.
- [22] Y. Lin, D. Gritsenko, S. Feng, Y. C. Teh, X. Lu, J. Xu, *Biosens. Bioelectron.* **2016**, *83*, 256.
- [23] M. Wang, Z. Song, Y. Jiang, X. Zhang, L. Wang, H. Zhao, Y. Cui, F. Gu, Y. Wang, G. Zheng, *Anal. Bioanal. Chem.* **2021**, *12*, 3299.
- [24] J. P. Devadhasan, J. Kim, *Sens. Actuators, B* **2018**, *273*, 18.
- [25] M. Medina-Sánchez, M. Cadevall, J. Ros, A. Merkoçi, *Anal. Bioanal. Chem.* **2015**, *28*, 8445.
- [26] S. Nishat, A. T. Jafry, A. W. Martinez, F. R. Awan, *Sens. Actuators, B* **2021**, *336*, 129681.
- [27] L. M. Hillscher, V. J. Liebich, O. Avrutina, M. Biesalski, H. Kolmar, *ChemTexts* **2021**, *2*, 14.
- [28] A. Böhm, F. Carstens, C. Trieb, S. Schabel, M. Biesalski, *Microfluid. Nanofluid.* **2014**, *5*, 789.
- [29] Ç. K. Söz, S. Trosien, M. Biesalski, *ACS Mater. Lett.* **2020**, *4*, 336.
- [30] A. Ghosh, R. Ganguly, T. M. Schutzius, C. M. Megaridis, *Lab Chip* **2014**, *9*, 1538.
- [31] L. Rivas, M. Medina-Sánchez, A. de La Escosura-Muñiz, A. Merkoçi, *Lab Chip* **2014**, *22*, 4406.
- [32] C. Dubois, N. Herzog, C. Rüttiger, A. Geißler, E. Grange, U. Kunz, H.-J. Kleebe, M. Biesalski, T. Meckel, T. Gutmann, M. Gallei, A. Andrieu-Brunsen, *Langmuir* **2017**, *1*, 332.
- [33] W. Chen, H. He, H. Zhu, M. Cheng, Y. Li, S. Wang, *Polymers (Basel)* **2018**, *10*, 592.
- [34] S. Jiang, S. Zhou, B. Du, R. Luo, *ACS Omega* **2021**, *24*, 16016.
- [35] Y. Guan, B. Sun, *Microsyst. Nanoeng.* **2020**, *6*, 14.
- [36] T. Tian, Y. Bi, X. Xu, Z. Zhu, C. Yang, *Anal. Methods* **2018**, *29*, 3567.
- [37] S. B. Berry, S. C. Fernandes, A. Rajaratnam, N. S. DeChiara, C. R. Mace, *Lab Chip* **2016**, *19*, 3689.
- [38] M. M. Thuo, R. V. Martinez, W.-J. Lan, X. Liu, J. Barber, M. B. J. Atkinson, D. Bandarage, J.-F. Bloch, G. M. Whitesides, *Chem. Mater.* **2014**, *14*, 4230.
- [39] B. Kalish, M. K. Tan, H. Tsutsui, *Micromachines (Basel)* **2020**, *11*, 773.
- [40] C.-A. Chen, W.-S. Yeh, T.-T. Tsai, Y.-D. Li, C.-F. Chen, *Lab Chip* **2019**, *4*, 598.
- [41] N. Colozza, K. Kehe, G. Dionisi, T. Popp, A. Tsoutsouloupoulos, D. Steinritz, D. Moscone, F. Arduini, *Biosens. Bioelectron.* **2019**, *129*, 15.
- [42] H. Liu, Y. Xiang, Y. Lu, R. M. Crooks, *Angew. Chem.* **2012**, *28*, 7031.
- [43] H. Yang, Y. Zhang, L. Li, L. Zhang, F. Lan, J. Yu, *Anal. Chem.* **2017**, *14*, 7511.
- [44] N. M. Neris, R. D. Guevara, A. Gonzalez, F. A. Gomez, *Electrophoresis* **2019**, *2*, 296.
- [45] X. Li, X. Liu, *Adv. Healthcare Mater.* **2016**, *11*, 1326.
- [46] J. Ding, B. Li, L. Chen, W. Qin, *Angew. Chem., Int. Ed. Engl.* **2016**, *42*, 13033.
- [47] H. Liu, R. M. Crooks, *J. Am. Chem. Soc.* **2011**, *44*, 17564.
- [48] P. Rattanarat, W. Dungchai, D. Cate, J. Volckens, O. Chailapakul, C. S. Henry, *Anal. Chem.* **2014**, *7*, 3555.
- [49] Y. Wang, S. Sun, J. Luo, Y. Xiong, T. Ming, J. Liu, Y. Ma, S. Yan, Y. Yang, Z. Yang, J. Reboud, H. Yin, J. M. Cooper, X. Cai, *Microsyst. Nanoeng.* **2020**, *6*, 32.
- [50] Y.-R. Zhang, J.-T. Chen, B. Hao, R. Wang, P.-C. Ma, *Carbohydr. Polym.* **2020**, *240*, 116318.
- [51] W. Zhu, W. Huang, W. Zhou, Z. Qiu, Z. Wang, H. Li, Y. Wang, J. Li, Y. Xie, *Carbohydr. Polym.* **2020**, *245*, 116587.
- [52] W. Zhang, P. Lu, L. Qian, H. Xiao, *Chem. Eng. J.* **2014**, 431.
- [53] J. B. You, Y. Yoo, M. S. Oh, S. G. Im, *ACS Appl. Mater. Interfaces* **2014**, *6*, 4005.

- [54] Y. Zhang, T. Ren, J. He, *ACS Appl. Mater. Interfaces* **2018**, *13*, 11343.
- [55] M. Nau, N. Herzog, J. Schmidt, T. Meckel, A. Andrieu-Brunsen, M. Biesalski, *Adv. Mater. Interfaces* **2019**, *18*, 1900892.
- [56] S. Bump, A. Böhm, L. Babel, S. Wendenburg, F. Carstens, S. Schabel, M. Biesalski, T. Meckel, *Cellulose* **2015**, *1*, 73.
- [57] D. R. Dunphy, P. H. Sheth, F. L. Garcia, C. J. Brinker, *Chem. Mater.* **2015**, *1*, 75.
- [58] J. Schindelin, I. Arganda-Carreras, E. Frise, V. Kaynig, M. Longair, T. Pietzsch, S. Preibisch, C. Rueden, S. Saalfeld, B. Schmid, J.-Y. Tinevez, D. J. White, V. Hartenstein, K. Eliceiri, P. Tomancak, A. Cardona, *Nat. Methods* **2012**, *7*, 676.